

**Highly separated transitional shock-wave/boundary-layer interactions
A spatial modal study**

Nel, Philipp L.; Schreyer, Anne Marie; Schrijer, Ferry F.J.; van Oudheusden, Bas W.; Swoboda, Marius

DOI

[10.1063/5.0239390](https://doi.org/10.1063/5.0239390)

Publication date

2024

Document Version

Final published version

Published in

Physics of Fluids

Citation (APA)

Nel, P. L., Schreyer, A. M., Schrijer, F. F. J., van Oudheusden, B. W., & Swoboda, M. (2024). Highly separated transitional shock-wave/boundary-layer interactions: A spatial modal study. *Physics of Fluids*, 36(11), Article 116114. <https://doi.org/10.1063/5.0239390>

Important note

To cite this publication, please use the final published version (if applicable).
Please check the document version above.

Copyright

Other than for strictly personal use, it is not permitted to download, forward or distribute the text or part of it, without the consent of the author(s) and/or copyright holder(s), unless the work is under an open content license such as Creative Commons.

Takedown policy

Please contact us and provide details if you believe this document breaches copyrights.
We will remove access to the work immediately and investigate your claim.

Green Open Access added to TU Delft Institutional Repository





'You share, we take care!' - Taverne project

<https://www.openaccess.nl/en/you-share-we-take-care>

Otherwise as indicated in the copyright section: the publisher is the copyright holder of this work and the author uses the Dutch legislation to make this work public.

RESEARCH ARTICLE | NOVEMBER 05 2024

Highly separated transitional shock-wave/boundary-layer interactions: A spatial modal study

Philipp L. Nel ; Anne-Marie Schreyer ; Ferry F. J. Schrijer ; Bas W. van Oudheusden ; Marius Swoboda



Physics of Fluids 36, 116114 (2024)

<https://doi.org/10.1063/5.0239390>



View
Online



Export
Citation

Articles You May Be Interested In

Assimilating mean velocity fields of a shockwave–boundary layer interaction from background-oriented schlieren measurements using physics-informed neural networks

Physics of Fluids (July 2024)

Large eddy simulation of shock wave/boundary layer interactions in a transonic compressor cascade

Physics of Fluids (July 2024)

Experimental investigation of primary and corner shock boundary layer interactions at mild back pressure ratios

Physics of Fluids (August 2016)



Physics of Fluids

Special Topics Open
for Submissions

[Learn More](#)

Highly separated transitional shock-wave/boundary-layer interactions: A spatial modal study

Cite as: Phys. Fluids **36**, 116114 (2024); doi: [10.1063/5.0239390](https://doi.org/10.1063/5.0239390)

Submitted: 19 September 2024 · Accepted: 16 October 2024 ·

Published Online: 5 November 2024



View Online



Export Citation



CrossMark

Philipp L. Nel,^{1,a)} Anne-Marie Schreyer,¹ Ferry F. J. Schrijer,^{2,b)} Bas W. van Oudheusden,² and Marius Swoboda³

AFFILIATIONS

¹RWTH Aachen University, Templergraben 55, Aachen 52062, Germany

²Faculty of Aerospace Engineering, Delft University of Technology, Kluyverweg 1, Delft 2629 HS, the Netherlands

³Rolls-Royce Germany Ltd. & Co. KG, Blankenfelde-Mahlow, Brandenburg 15827, Germany

^{a)}Author to whom correspondence should be addressed: nel@ist.rwth-aachen.de

^{b)}Electronic mail: f.f.schrijer@tudelft.nl

ABSTRACT

At cruise altitudes, the Reynolds number may become sufficiently low to allow a laminar boundary layer to persist on the suction side of a transonic fan blade up to the shock-wave/boundary-layer interaction (SBLI). In such a transitional SBLI with sufficiently large shock-induced separation, a shock oscillation mechanism occurs, with the source at the upstream growth (until a critical length) and natural suppression (through shear layer instabilities) of the separation bubble. The oscillation cycle is characterized by a temporarily vanishing upstream laminar part of the separation bubble. The suppression of this laminar part is accompanied by downstream advection of turbulence and subsequent entrainment into the bulk separation bubble, affecting the reflected shock movement. In order to study the spatial behavior of the mechanism, particle image velocimetry of a highly separated transitional oblique SBLI at Mach 2.3 is conducted in the high speed aerodynamics laboratory of Delft University of Technology. Statistical quantities, including root mean square velocity fluctuations, phase averages, and spatial modes from proper orthogonal decomposition, are investigated. The entrainment strength varies depending on the phase of the oscillation, and the turbulent shear layer is not fully developed. The main growth and shrinking mode of the separation bubble were extracted, which affects the slip line region size and shock position. Secondary modes that affect the shear layer undulation and upstream effects were also extracted. The study provides quantitative analyses of an important shock oscillation type, with the focus on capturing the separation bubble size variation and upstream effects.

Published under an exclusive license by AIP Publishing. <https://doi.org/10.1063/5.0239390>

I. INTRODUCTION

Reynolds numbers at cruise altitude on transonic fans of smaller engine sizes, such as those of business jets, can be low enough to result in a laminar boundary layer persisting on the suction side of the fan blade up to the shock-wave/boundary-layer interaction (SBLI). With the increasing loading of transonic fan blades,^{1,2} there is a growing interest in studying strong transitional SBLIs.³ In a previous work of the authors,⁴ it was shown that the shock oscillation mechanism present in transonic fans at altitude can be studied in a canonical research configuration, which turned out to be a highly separated transitional oblique SBLI in which transition occurs on the separated shear layer upstream of the shock. In the current study, we aim to further quantify the behavior of the upstream section of the separation bubble (which

causes the shock oscillation mechanism), the bulk separation bubble size variation, Mach stem, and reflected shock in this highly separated transitional SBLI.

Transitional SBLIs are a type of interaction with an oncoming laminar boundary layer, where it is emphasized that transition of the boundary layer occurs at the shock interaction itself (mostly as a result of it). Transitional SBLIs exhibit unsteadiness with fundamentally different mechanisms than laminar SBLIs and turbulent SBLIs.⁵

Babinsky and Harvey⁶ discuss transitional SBLIs, particularly in the context of hypersonics. At hypersonic flight at high altitudes, where the ambient density is low, high Mach numbers and low Reynolds numbers can lead to fully laminar SBLIs. However, as a vehicle descends during reentry, the Reynolds number increases, causing the

boundary layer to transition from laminar to turbulent within the interaction region. Once transition occurs, it significantly impacts the interaction by introducing turbulence and instabilities, leading to a more complex interaction, which is not well understood. As the transition progresses further upstream, it can reach the separation region, potentially reducing the separated zone or eliminating it altogether if the shock strength is insufficient.

When studying oblique SBLIs, the choice of flow deflection angle determines the strength of the interaction and the extent of boundary layer separation. Deflection angles can range from, e.g., 1° to 25° , depending on the Mach number and desired interaction strength. Low deflection angles, around 1° to 10° , are most often studied and are relatively weak interactions where only slight boundary layer thickening occurs.^{6,7} Moderate angles between 10° and 15° are employed to study interactions where boundary layer separation is more pronounced, often marking the transition from incipient to full separation.⁸ Higher deflection angles, ranging from 15° to 25° , are used to create strong shock-induced interactions, characterized by large separation bubbles and potentially highly unsteady shock behavior.⁹ However, as is usual in SBLI research, the focus is on turbulent shock-wave/boundary-layer interactions, as this is most often the case in practice.^{10–12}

In a transitional SBLI with sufficiently large shock-induced separation, a shock oscillation mechanism occurs, characterized by the growth and natural suppression of the upstream laminar part of the separation bubble.^{3,4} The suppression of this laminar part is accompanied by downstream advection of turbulence and subsequent entrainment into the bulk separation bubble, affecting the reflected shock movement. This interaction has been studied experimentally at Mach 2.3 in the High Speed Aerodynamics Laboratory at Delft University of Technology using particle image velocimetry (PIV). In a previous study by the authors,⁵ high-speed Schlieren imaging at 100 kHz and spark light shadowgraphy was used to study the transition and oscillation mechanics. A characteristic length scale based on the distance the periodically upstream propagating (laminar) separation shock travel was proposed, as this was found to be the source of the shock oscillation mechanism. The shock oscillation mechanism can be suppressed by tripping the boundary layer. Furthermore, the study validated large eddy simulations (LES) simulations with experimental results with regard to the dynamics, showing matching Strouhal frequencies.⁵ Spark light shadowgraphs confirmed the shifting transition location observed in LES. Numerical simulations indicated a strong dependency on free stream turbulence levels. Dominant shock oscillation frequencies shifted significantly to lower values for the turbulent interaction. Dynamic mode decomposition showed distinct mode shapes for the laminar vs turbulent interaction, with the laminar SBLI oscillation mode strongly linked to the separation bubble and upstream laminar separation shock. However, capturing the separation bubble size variation and separating the sidewall from mid span flow was not possible with Schlieren imaging. A PIV study on the canonical research configuration⁴ aims to further the understanding of this shock oscillation mechanism by quantitative measurements and spatial modal analysis at the mid-span plane.

In Sec. II, we introduce the experimental setup and the methods employed for the analysis. Section III provides a presentation of the results, with raw data and statistical analyses of a separation bubble and upstream view of the flow field: In Sec. III A, we present the mean velocity components and root mean square (RMS) velocity

fluctuations of the separation bubble region. Section III B discusses the phase-averaged analysis of the flow, with an evaluation of the shear layer vorticity thickness. In Sec. III C, we present the spatial modal analysis using proper orthogonal decomposition (POD) for investigating flow structure variations in the separation bubble region. This also includes analyzing upstream effects, since the shock oscillation mechanism is rooted in the growth and collapse of the thin upstream laminar section of the separation bubble. The upstream analysis includes showing LES and spark light shadowgraphs from a concurrent investigation to corroborate. Finally, we conclude our findings in Sec. IV.

II. EXPERIMENTAL SETUP AND METHODS

The experimental setup is shown in Fig. 1. The tests were performed at $Ma = 2.3$ and $P_t = 2.8$ bar in the TST-27 blow down transonic/supersonic wind tunnel facility of the TU Delft. The wind tunnel has a cross section of $280\text{ mm} \times 280\text{ mm}$. A 19° shock generator was used. The resulting oblique shock wave impinges 6 cm from the leading edge of a flat plate. More details of the wind tunnel facility can be found in Giepmans.⁷ The specific model setup is described by Nel *et al.*⁵

A. Particle image velocimetry

Different parts of the mid span flow (see Fig. 2) were captured with a high resolution (1624×1236 , 130 pix/mm) Lavision Imager LX camera, equipped with a 105 mm Nikon Nikkor lens. The flow was seeded with DEHS particles (response time $\tau_p = 2\text{ }\mu\text{s}$), which are illuminated with a double-pulse YAG Spectra Physics Quanta Ray PIV-laser ($0.65\text{ }\mu\text{s}$ pulse separation and 400 mJ per pulse). The laser beam is guided into a downstream probe, which delivers the light sheet with a thickness of 1.5 mm to the test section. Figure 3 shows some photographs of the experimental setup with laser turned on.

Different fields of view (Fig. 2) are captured: an overview (Fig. 4) of the flow field shows the interaction region, as well as impinging and leading edge shock waves (26.2 pix/mm, 1 100 snapshots). In addition, a zoomed downstream view on the interaction region (45.75 pix/mm) shows the bulk of the separation bubble (1 200 snapshots) and an upstream zoomed view captures compression waves from the thin upstream laminar part of the separation bubble (400 snapshots). This

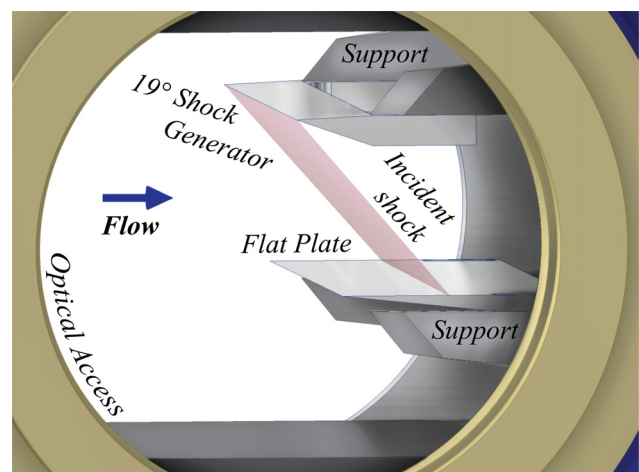


FIG. 1. Model in experimental setup of TU Delft TST-27 transonic/supersonic wind tunnel.

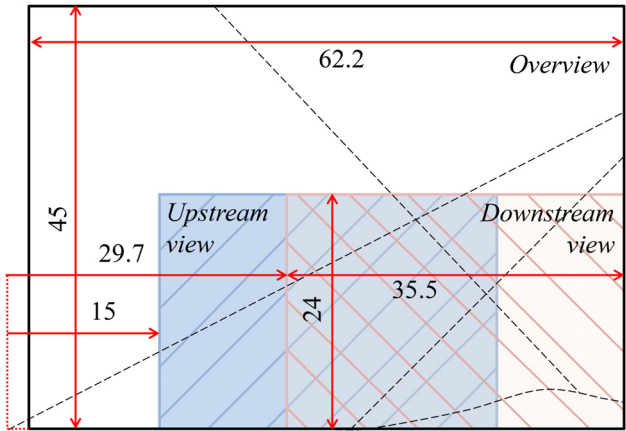


FIG. 2. Three fields of view for the PIV with simplified flow structure: measurements from the leading edge and flat plate surface in mm.

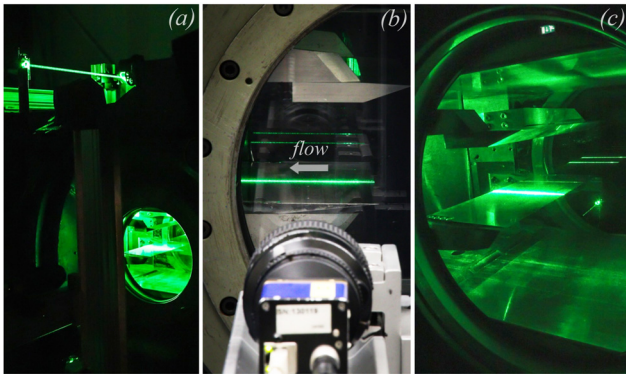


FIG. 3. PIV setup: (a) illumination is provided from downstream of the test section (flow right to left). (b) Camera directed at the test section. (c) Close-up of the test section with the light sheet at mid-span, showing the laser light source.

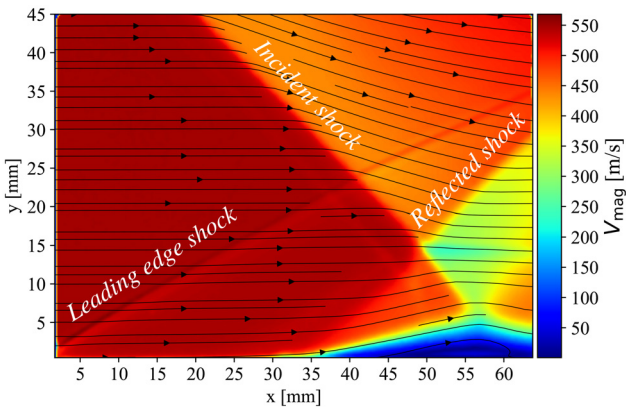


FIG. 4. Experimental setup: time-averaged PIV velocity magnitude in an overview of the flow field, showing leading edge shock, impinging and reflected shocks, compression wave region at shock foot, closed separation bubble, and a Mach stem signature.

TABLE I. Summary of uncertainty analysis.

Uncertainty source	Error
Statistical (ϵ_u)	$\leq 0.9\%$
Statistical (ϵ_v)	$\leq 0.2\%$
Cross-correlation (ϵ_{cc})	$\leq 0.6\%$
Particle slip (ϵ_{slip})	$\leq 18\%$

upstream part periodically vanishes due to suppression from turbulence formed by instabilities during the upstream growth of the laminar part.

Vector processing is performed using LaVision DaVis with the multi-pass ($64 \times 64 \rightarrow 16 \times 16$) approach, utilizing adaptive PIV weighting to better capture gradients.

B. Spatial modal analysis

The triple decomposition method¹³ is used to analyze the spatial behavior of the flow. This method separates the flow field into three components: the mean flow (time-averaged component), the coherent structures (organized component), and the incoherent fluctuations (stochastic component). The flow field $\mathbf{u}(x, t)$ is expressed as the sum of these components,

$$\mathbf{u}(x, t) = \mathbf{U}(x) + \mathbf{u}'(x, t) + \mathbf{u}''(x, t),$$

where $\mathbf{U}(x)$ is the mean flow, $\mathbf{u}'(x, t)$ represents the coherent structures, and $\mathbf{u}''(x, t)$ denotes the incoherent fluctuations. The proper orthogonal decomposition (POD) is used to identify and extract the coherent structures by solving an eigenvalue problem for the covariance matrix of the fluctuations. This decomposition is used to understand the effect of the dominant modes on the flow structure. The PIV data can be projected onto the extracted modes to obtain the time coefficients, and the effect of a specific mode (or modes) on the flow can be evaluated by weighting the mode by its time coefficient.

C. Post-processing algorithm

In the supersonic experiments, sporadic large areas with low seeding density necessitate post-processing to identify and eliminate

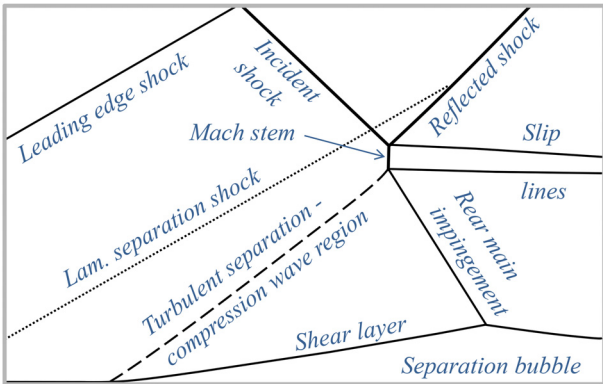


FIG. 5. Nomenclature of SB LI flow features.

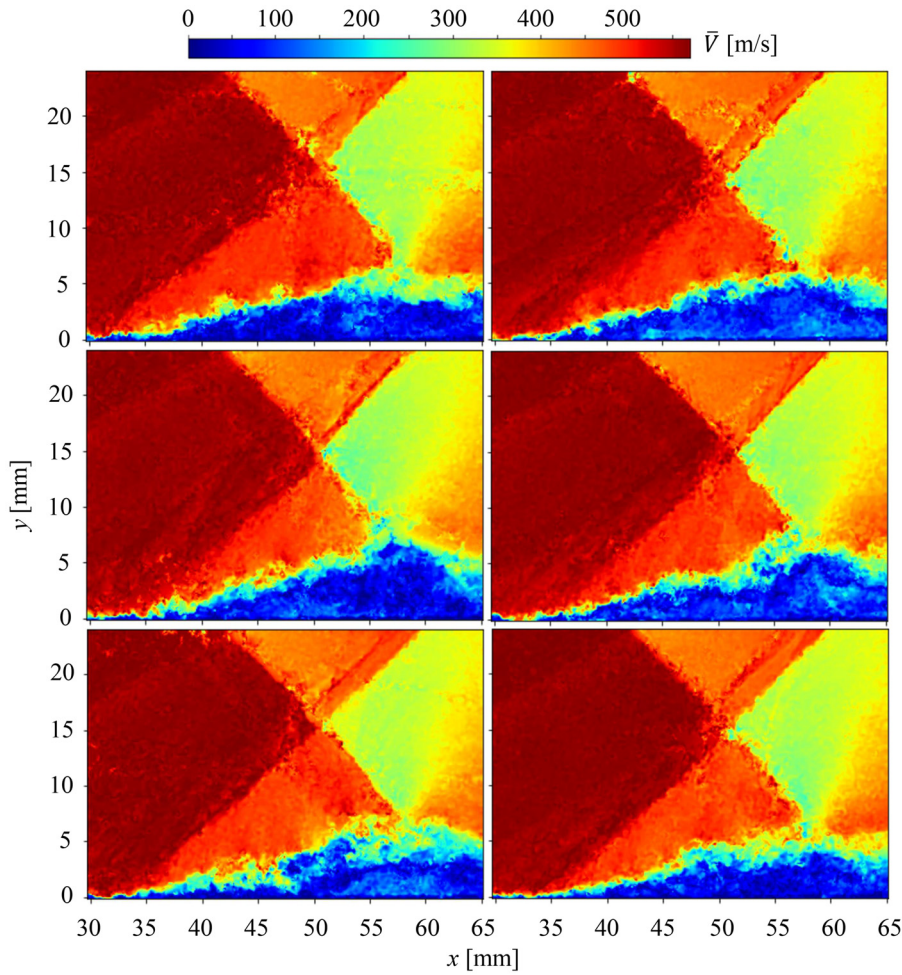


FIG. 6. Example PIV snapshots showing regular reflection state.

these areas, characterized by logically unnatural gradients and unresolved clusters. This step ensures a cleaner input for the analysis, resulting in more accurate standard deviations and modes from proper orthogonal decomposition (POD).

Additionally, post-processing avoids the need for larger interrogation windows during vector processing, which is important for gaining accurate insights into the instantaneous flow field.

As a first iteration of outlier replacement, the universal outlier detection algorithm by Westerweel and Scarano¹⁴ is applied to get rid of spurious vectors with a replacement based on the local median. As a standard deviation filter, an additional step of outlier replacement is done based on the best correlating automatically calculated phase average. In a final iteration, the identified outlier clusters of the standard deviation test are based on a proper orthogonal decomposition lower order reconstruction of the specific image at hand. The automatically computed phase-averaged vector fields are based on maximizing the differences between calculated averaged phases.

The Pearson correlation matrix C is calculated between each image and all other images,

$$C_{ij} = r(q_i, q_j) = \frac{\sum_k (q_i[k] - \bar{q}_i)(q_j[k] - \bar{q}_j)}{\sqrt{\sum_k (q_i[k] - \bar{q}_i)^2 \sum_k (q_j[k] - \bar{q}_j)^2}}.$$

Images are sorted according to the average correlations of each image with all other images,

$$r_i^{\text{avg}} = \frac{1}{N} \sum_{j=1}^N C_{ij}.$$

From this list, we select the largest gaps (n phases). This leads to the identification of reference images R capturing maximum variability. Subsequently, the correlation of each image with each determined reference image R is computed,

$$C_{i,j} = r(q_i, R_j).$$

Each image is assigned the phase number of the reference image with which it has the highest correlation, and reference phase averaged images R can be computed.

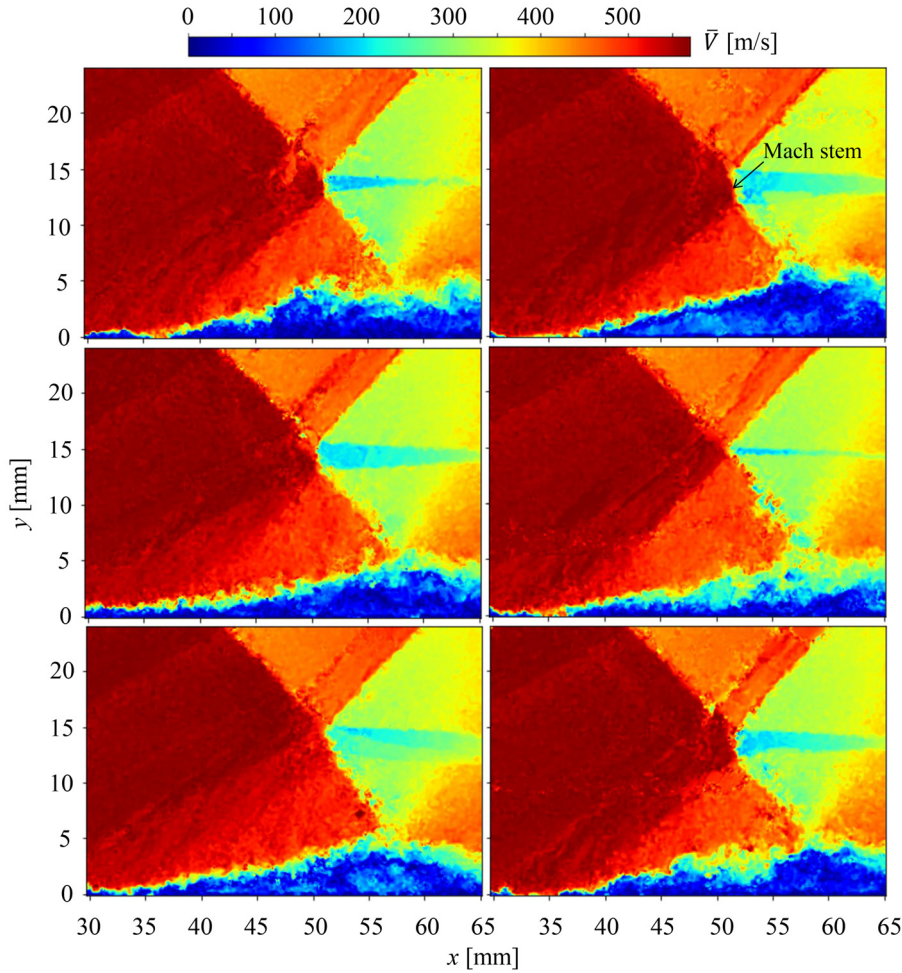


FIG. 7. Example PIV snapshots showing Mach reflection state.

For outlier replacement, the phase averaged image R' with which a specific image I has the highest correlation r is used for outlier replacement of that image,

$$r = \frac{\sum_{i=1}^n (I_i - \bar{I})(R'_i - \bar{R}')}{\sqrt{\sum_{i=1}^n (I_i - \bar{I})^2 \sum_{i=1}^n (R'_i - \bar{R}')^2}}.$$

Outliers are marked based on whether a vector falls outside a specified range (relative to the mean plus and minus the standard deviation). For a cluster of outliers, weighted replacement is performed using weight matrix W for replacement, defined by exponential decay,

$$W_{dy,dx} = \exp\left(-\frac{S \cdot \sqrt{dy^2 + dx^2}}{r}\right),$$

where S is the transition strength and r is the radius of the replacement window.

Final outlier replacement of originally marked outliers is on values from a POD reconstruction using 20 modes calculated after the outlier replacement based on local median and phase averages. This involves solving the eigenvalue problem of the covariance matrix C ,

$$C = \frac{1}{N-1} \mathbf{X}^T \mathbf{X},$$

where X is the centered data matrix. The POD modes ϕ_k are the eigenvectors of C , and the temporal coefficients a_k are given by projecting the data onto the modes,

$$a_k = u(x, j) \phi_k.$$

In a final iteration, outlier clusters from the standard deviation test are replaced again, now using POD reconstructed snapshots from 20 modes,

$$u(x, j) = \bar{u}(x) + \sum_{k=1}^m a_{ik} \phi_k.$$

D. Uncertainty quantification

The uncertainties considered include statistical convergence uncertainty, particle slip velocity uncertainty, and cross correlation uncertainty. The separation bubble and especially the shock wave region exhibit significantly higher uncertainties than the free stream. For the u component, the highest uncertainty above the separation

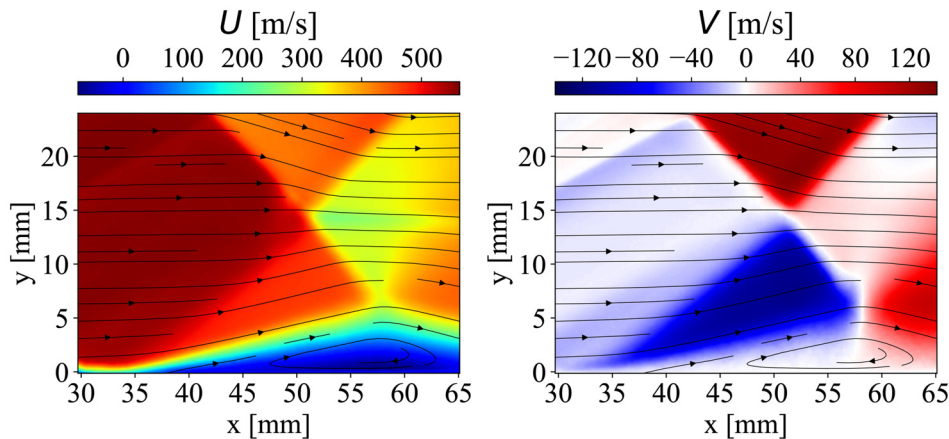


FIG. 8. Mean flow field for u (left) and v (right) components.

bubble occurs at the Mach stem region. Table I provides the uncertainties which were calculated as according to Melling¹⁵ and Sciacchitano and Wieneke,¹⁶ considering the shock wave region. The uncertainties are comparable with previous works utilizing PIV of high speed flows.^{7,17} Despite the low statistical and correlation uncertainties (0.2%–0.9%), the particle slip uncertainty of 18% limits direct quantitative conclusions from instantaneous velocity fields. Therefore, we focus on a phase-averaged and statistical approach. The shock waves present in the domain cause a sudden change in the refractive index of the air, which leads to blurring of the imaged tracer particles. While this may prohibit an analysis considering the exact instantaneous location of the shock wave, we rather base our conclusions on differences from statistics.

III. RESULTS

First, we discuss the overall flow topology. The nomenclature of the observed flow features is shown in Fig. 5. A Mach stem forms as a result of the strong SBLI. From the instantaneous snapshots of the separation bubble region (Figs. 6 and 7), we observe a movement of the reflected shock, a variation of the separation bubble size, the occurrence and vanishing of a Mach stem, and differences in the upstream behavior of the separation bubble, with some snapshots showing a distinct separation shock, and others showing a smeared compression

wave region or the signature of a laminar separation shock. This means that the interaction is switching between a laminar and a turbulent SBLI due to the way in which transition on the upstream shear layer of the separation bubble periodically washes away the upstream laminar section of the separation bubble.⁵ Through the course of the shock oscillation, the Mach stem temporarily vanishes if the reflected shock and separation shock align, with the interaction switching between a regular reflection and a Mach reflection type. This is illustrated by comparing the instantaneous snapshots of Fig. 6 with Fig. 7. It would appear that the Mach stem generally exists for a shallow separation bubble—this is to be examined using phase averaging and POD (see Sec. III C).

A. Separation bubble mean and velocity fluctuations

The mean u and v components of the bulk separation bubble region are shown in Fig. 8. The root mean square (RMS) velocity fluctuations (Fig. 9) indicate that the nondimensionalized u and v RMS velocity components do not reach values of 0.2 and 0.15, respectively. Hence, a fully developed turbulent separated shear layer¹⁸ is not achieved in this interaction. Values of u'_{rms}/u_∞ are relatively high (0.2–0.3) in the shear layer before the main shock impingement, and start to diminish to 0.15 after this point. Conversely, the values for the

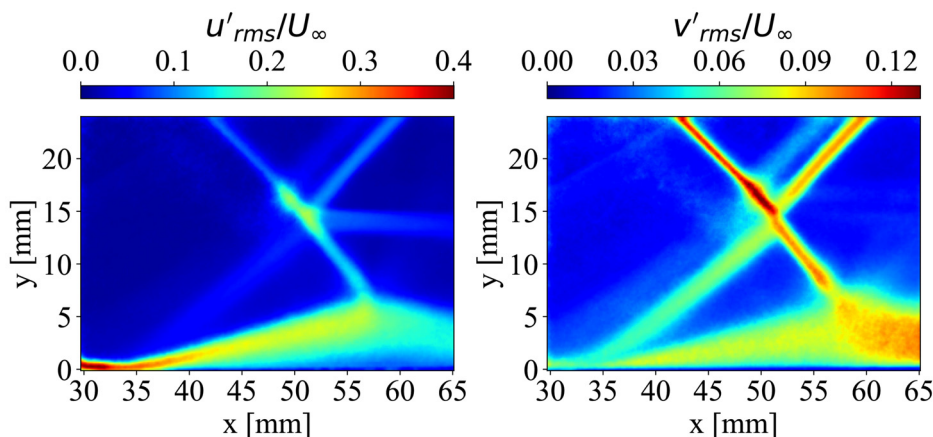


FIG. 9. Root mean square (RMS) velocity fluctuations of the u (left) and v (right) components.

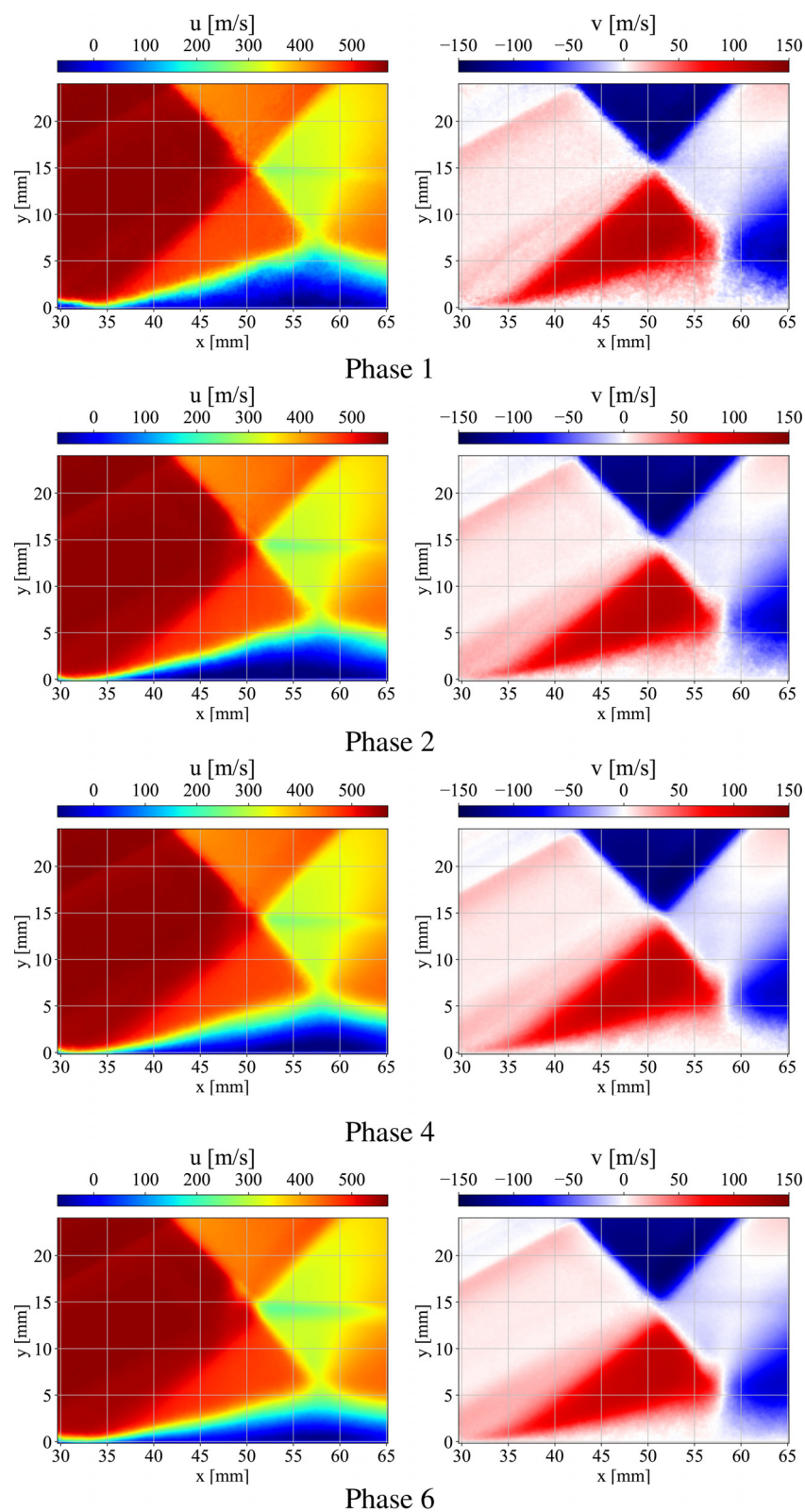


FIG. 10. Phase averages: u (left) and v (right) components.

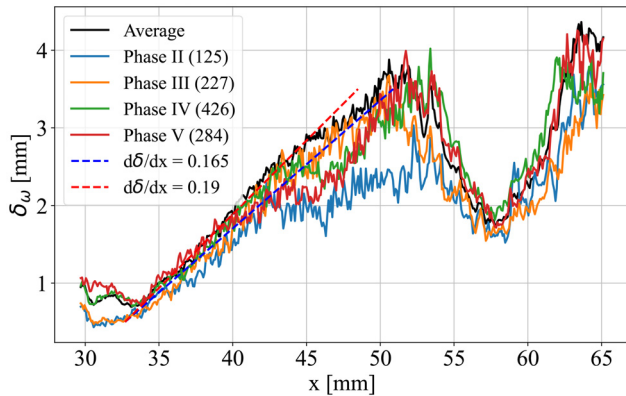


FIG. 11. Vorticity thickness of main (middle) phases. Number of snapshots indicated in brackets.

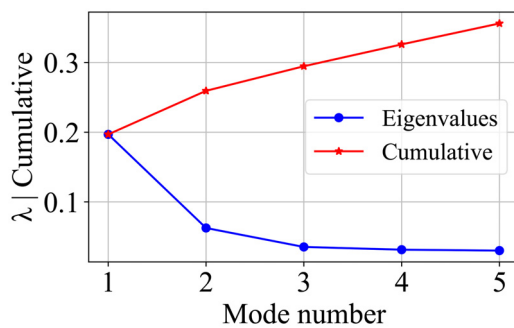


FIG. 12. Separation bubble region: eigenvalue significance.

transverse component v'_{rms}/u_{∞} are relatively low upstream of the main impingement (0.07–0.08), with vertical mixing abruptly increasing to 0.10 afterward.

B. Phase averaged analysis

In order to evaluate the different phases of the shock oscillation cycle, the phase identification part of the post-processing algorithm is

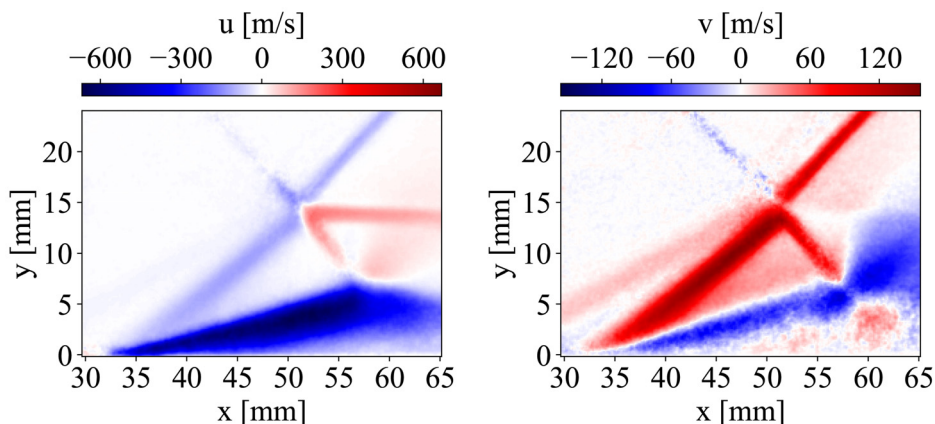


FIG. 13. Downstream POD mode 1: u component (left) and v component (right).

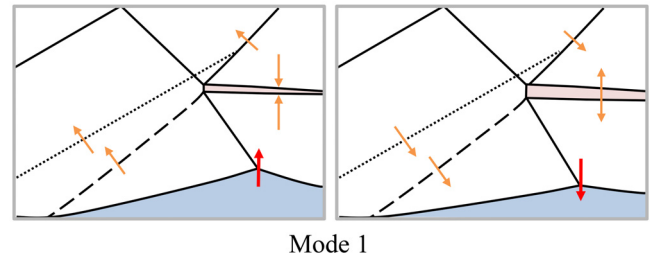


FIG. 14. Downstream analysis: effect of first mode on flow features.

repeated on the post-processed data to obtain six phase averages, of which the four most important are shown in Fig. 10. Phase 1 corresponds to the highest separation bubble where the reflected shock is positioned upstream, whereas phase 6 exhibits the shallowest separation bubble where the reflected shock is downstream. It is shown that phase 1 exhibits an almost concave upstream part of the separation bubble and a steep separation angle, with the flow field featuring more closely spaced compression waves at the base of the separation bubble relative to phase 6. Furthermore, an upstream positioning of the reflected shock is observed for phase 1, and a downstream positioning for phase 6. The slip line region is thicker for phase 6, indicative of a larger Mach stem.

Comparing phase 2 and phase 4, it is apparent that phase 2 features a thinner shear layer in the part of the separation bubble upstream of the shock than phase 4. This suggests that entrainment differs in different parts of the separation bubble, depending on the phase. This corresponds to previous findings,^{4,5} where it was seen that the separation bubble is periodically suppressed by periodically forming upstream instabilities. The differences in shear layer vorticity thickness¹⁹ for different phases, as well as for the average, can be seen in Fig. 11.

Note that the time averaged result in Fig. 11 follows a shear layer vorticity thickness growth rate between 0.19 and 0.165, which compares with findings of other studies with compressible shear layers.^{19,20} Phase 2 has a lower initial shear layer growth rate than the other phases, but exhibits a similar vorticity thickness after the impinging shock wave. Phase 3 exhibits a higher growth rate upstream of the shock, but a relatively low vorticity thickness downstream of the shock.

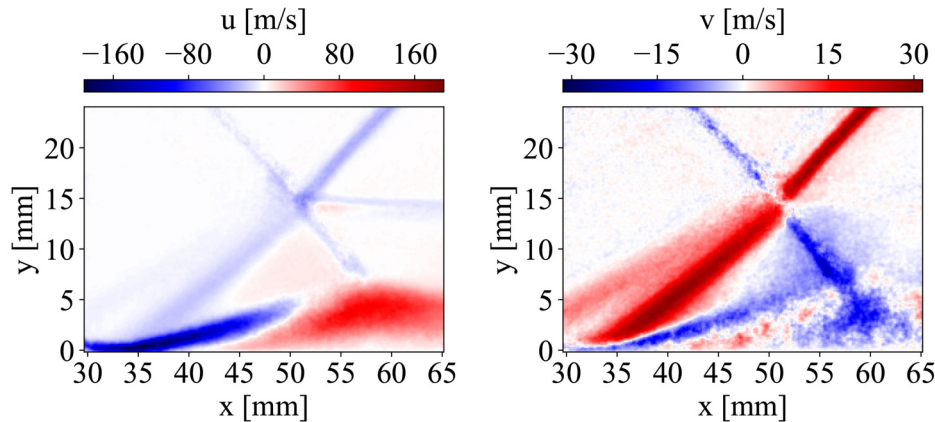


FIG. 15. Downstream POD mode 2: u component (left) and v component (right).

These findings indicate clear differences in the entrainment strength between the phases and suggest that instabilities of different size are transported downstream, depending on the phase. This implies that some phases exhibit a more turbulent shear layer than others, which corroborates previous findings where it was seen that the oscillation mechanism source depends on instabilities, which are generated on a periodically vanishing upstream laminar section of the separation bubble.⁵ These findings also make sense with respect to the finding that the shear layer is not a fully developed turbulent shear layer, as suggested in the analysis of RMS velocity fluctuations (Sec. III A).

C. Results: Spatial modal analysis

Using the decomposition method described in Sec. II B, we analyze the coherent spatial modes that dominate the unsteady flow field to understand the separation bubble size variation and subtle upstream-growing effects of the separation bubble, which are the source of the shock oscillation. We focus on the first two modes, as they are the most dominant. This is demonstrated by the significance of their eigenvalues (Fig. 12). Consequently, we analyze the effect of these two modes on the flow field.

1. Bulk separation bubble

The u and v components of the first mode are shown in Fig. 13. The mode displays the main growing and shrinking of the separation bubble. The positive u velocity in the slip line region, coupled by a negative velocity in the separation bubble, means that the slip line vanishes when the separation bubble size increases. Hence, the disappearance of

the Mach stem is linked to a larger separation bubble. This is also clear in the phase averages, where for the first phase, displaying the largest separation bubble, the slip line is barely visible in comparison with the sixth phase, which displays the smallest separation bubble. This was confirmed by evaluating the effect of the first mode using the time coefficients of the modes. The effect of the first mode is schematically shown in Fig. 14. The negative u velocity and positive v in the separation shock and reflected shock region indicate an upstream movement of these shock waves when the separation bubble has grown. The first mode confirms that the Mach stem generally exists for a shallow separation bubble.

The second POD mode shape, shown in Fig. 15, is the first mode associated with an undulation of the separated shear layer. The effect on the flow structure can be seen in Fig. 16. Even though the v component shape is almost the same as for the first mode, it is clear that the effect on the most upstream compression waves is more pronounced in the second mode. This is logical because, for the u component, the negative part reaches further upstream than the upstream reach of the first mode. Contrary to the first mode, the second mode is not associated with a slip line/Mach stem size variation. Both the first and second modes affect the laminar separation shock, compression waves from turbulent thickening, and reflected shock.

2. Upstream effects and oscillation mechanism

Upstream of the shock impingement, subtle yet important phenomena for the overall behavior of the shock oscillation occur, which

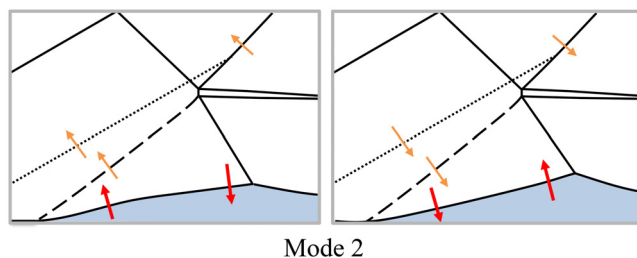


FIG. 16. Downstream analysis: effect of second mode on flow features.

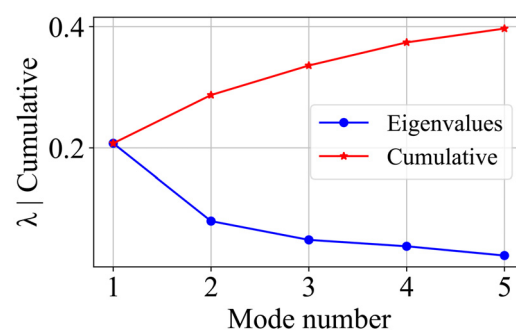


FIG. 17. Upstream region: eigenvalue significance.

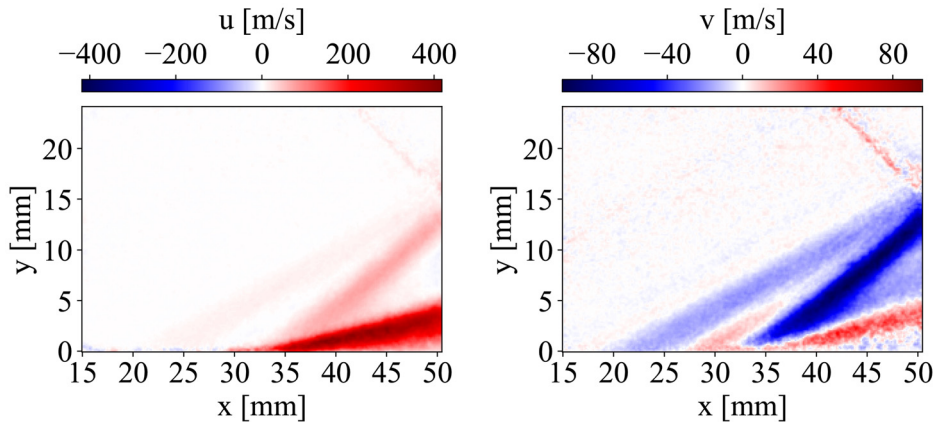


FIG. 18. Upstream POD mode 1: u component (left) and v component (right).

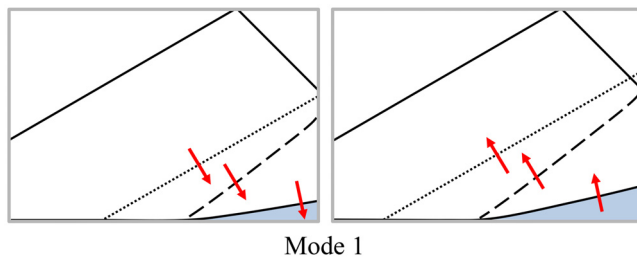


FIG. 19. Upstream analysis: effect of first mode on flow features.

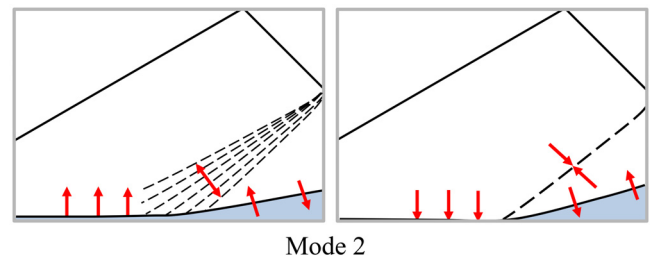


FIG. 21. Upstream analysis: effect of second mode on flow features.

we further characterize by POD analysis of the upstream view (see Fig. 2). The origin of the shock oscillation mechanism can be found in the upstream laminar part of the separation bubble. This thin and long section of the separation bubble grows in the upstream direction but carries with it instabilities on the shear layer. At a certain critical length, these instabilities are turbulent too far upstream and cut off the laminar part of the separation bubble, causing a collapse of the separation bubble as a whole due to the generated entrainment eddies advecting downstream.^{4,5} Therefore, we focus on an upstream analysis next.

With regard to the eigenvalue significance of the upstream modes (Fig. 17), we see a slightly higher influence of the second mode when compared to the modes extracted over the separation bubble region.

The first mode shape (Fig. 18) is of the same type as for the separation bubble region and corresponds to the mode type of Fig. 13. The separation bubble growth (significant positive velocity shown in the mode shape of the u component) causes an outward movement of the compression waves caused by turbulent thickening, as well as the separation shock from the upstream (laminar) edge of the separation bubble. Figure 19 shows this effect, and it is analogous to the finding previously shown on the bulk separation bubble region modes. However, in the upstream analysis, the difference of the first and second POD modes on the upstream compression waves is now clearly pronounced, due to the upstream focus rather than the POD mode extraction being concentrated on the separation bubble region.

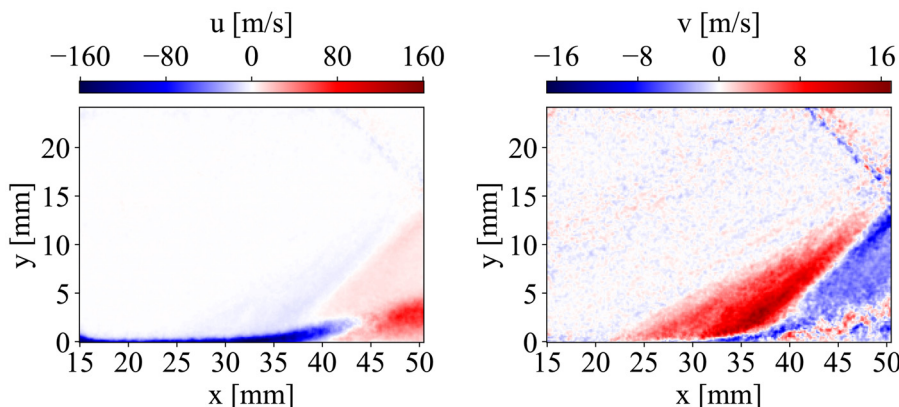


FIG. 20. Upstream POD mode 2: u component (left) and v component (right).

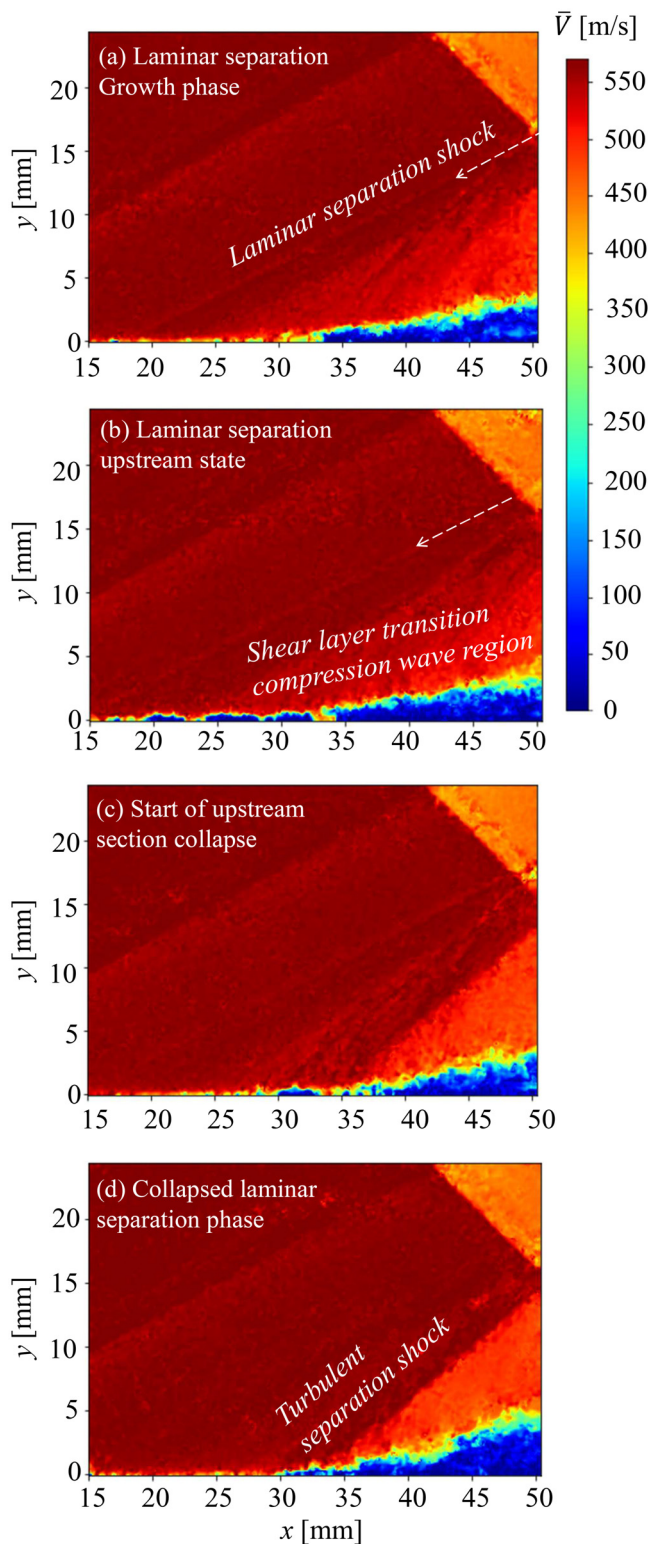


FIG. 22. Example PIV snapshots showing states of oscillation. Laminar separation shock (arrow) can be seen for upstream states.

The second POD mode (Fig. 20) shows a shear layer undulation as well as a boundary layer thickening (negative u component region close to wall) and is associated with a horizontal spreading of compression waves due to the transition of the boundary layer during the upstream growth phase of the separation bubble, which has also been observed in high speed Schlieren and spark light shadowgraphs.⁵ The resulting compression wave spreading is more clear in the v component mode shape.

There is a clear difference in the type of upstream effect in comparison with the first POD mode, in that the most upstream separation compression waves of the first mode (seen more clearly in v component of Fig. 18) originate from the laminar edge of the separation bubble, whereas the upstream edge of the compression waves region shown in the second POD mode of Fig. 20 originates from instabilities, which cause a shear layer thickening. This difference is also illustrated by the differing effects of the first (Fig. 19) and second (Fig. 21) modes on the flow features.

The described phenomena are also visible in instantaneous PIV snapshots (Fig. 22) depicting the states of the separation bubble throughout an oscillation cycle. The upstream phase of the oscillation, where a laminar separation shock exists and where a spread out compression wave region is visible, is shown in Figs. 22(a) and 22(b). In Fig. 22(c), the upstream section of the separation bubble starts to collapse. In the collapsed state, instabilities have advected downstream, the laminar section is temporarily suppressed, and the separation shock wave exhibits the typical form of a turbulent separation shock; this state is shown in 22(d). Spark light shadowgraphs⁵ offer insights to the instabilities on the shear layer, or the transition location. In the shadowgraph images (Fig. 23) sub-figure (a) shows the state where the laminar part of the separation bubble is growing in the upstream direction, and the instabilities can be seen on the separated shear layer. Figure 23(b) shows the state where the laminar section has started to collapse and 23(c) shows the collapsed state.

Large eddy simulations⁵ corroborate and confirm the findings. Figure 24 shows volumetric numerical shadowgraphs of the upstream region in an LES simulation. Snapshot (1) shows the state where the upstream laminar section is suppressed and starts to recover by snapshot (2). From snapshots (2) to (5), the laminar separation shock propagates upstream, originating from the laminar section of the separation bubble. In snapshots (6) and (7), the laminar part of the separation bubble collapses. Note the vertical downward movement of instabilities, which cut off the separation bubble region by entrainment. Snapshots (5) to (7) illustrate the coalescence of the compression wave region into a single shock wave as it retracts to the turbulent base of the separation bubble. By snapshot (7), the oscillation cycle restarts with the subsequent formation of a new laminar separation shock.

IV. CONCLUSIONS

To analyze the shock oscillation mechanism relevant in transonic fans of smaller engine size (business jet or defense type) at cruise altitude, we have performed statistical analyses on PIV results of a highly separated oblique shock-wave/boundary-layer interaction at Mach 2.3 with flow deflection angle of 19° . The oscillation mechanism has its source at the thin upstream laminar section of the separation bubble, which periodically collapses due to Kelvin–Helmholtz instabilities on this section, causing a downstream washing of turbulence and entrainment into the separation bubble, leading to a shock oscillation due to suppression of the

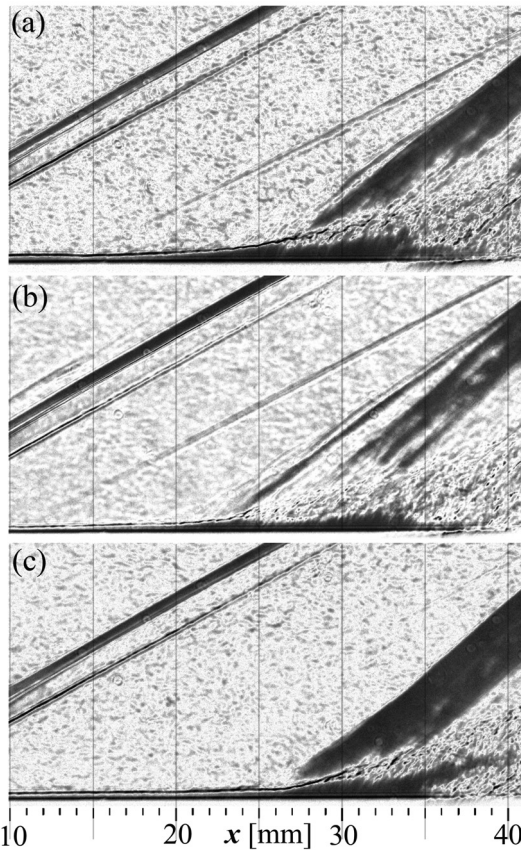


FIG. 23. Shadowgraphs showing growing (top), upstream (middle), and downstream (bottom) states of oscillation. Laminar separation shock can be seen for growing and upstream states.

bulk separation bubble. The study provides quantitative insights into the phenomena related to of this shock oscillation mechanism, with emphasis on the separation bubble size variation and upstream effects. The study builds on previous findings, where high-speed Schlieren imaging and spark light shadowgraphy were used to study transition and oscillation temporal dynamics.

The separation bubble shear layer does not reach a fully developed turbulent state, as shown by root mean square (RMS) velocity fluctuations. It was shown by instantaneous snapshots that there are states where a laminar separation shock is visible, and states where only a single (turbulent separation shock) exists. This complements previous studies, which evaluated the dynamics of the mechanism, by confirming this phenomenon at the mid plane section.

For a vertically grown separation bubble, there is a reduced slip line region thickness (shorter Mach stem), a more distinct separation shock upstream foot, as well as an upstream positioning of the reflected shock, as shown by phase averaged results and analysis of the first POD mode of the separation bubble (downstream view).

Differences in the entrainment strength between the phases suggest that instabilities of varying sizes are transported downstream depending on the phase, which have been confirmed through the

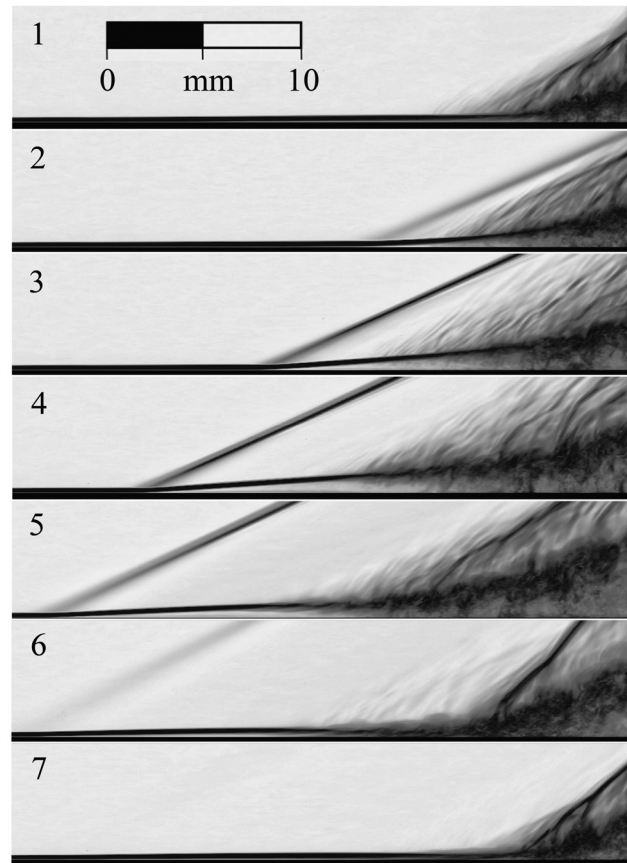


FIG. 24. Upstream view capturing growing and vanishing upstream section of separation bubble ($\Delta t = 6.9\text{e-}05\text{s}$). Numerical volumetric shadowgraph of LES with turbulence intensity of 0.07%.

analysis of the shear layer vorticity thickness. This is consistent with the observation that the shear layer is not a fully developed turbulent shear layer.

Proper orthogonal decomposition (POD) is used to extract coherent structures and their effects on the flow structure are analyzed. The first mode of the separation bubble region relates to the separation bubble size and also shows an effect on the slip line region size (Mach stem height increases for shallow separation), while the second mode is associated with shear layer undulations. Both first and second separation bubble region modes affect the shock wave positioning.

The upstream modal analysis showed a first mode analogous to that of the separation bubble region analysis, with the second mode highlighting the spreading of compression waves due to upstream boundary layer transition.

It is suggested that future work includes the application of high speed PIV on the laminar baseline case, for a comparison with various tripped configurations. Since with high speed Schlieren, it was not possible in previous studies to capture separation bubble size variation, such a study would provide additional spatiotemporal insights into the flow control aspect.

ACKNOWLEDGMENTS

The author participated in the TEAMAero project, which has received funding from the European Union's Horizon 2020 research and innovation programme under grant agreement No 860909.

AUTHOR DECLARATIONS

Conflict of Interest

The authors have no conflicts to disclose.

Author Contributions

Philipp L. Nel: Conceptualization (lead); Data curation (equal); Formal analysis (lead); Investigation (lead); Methodology (lead); Visualization (lead); Writing – original draft (lead). **Anne-Marie Schreyer:** Supervision (lead); Writing – review & editing (equal). **Ferry F. J. Schrijer:** Methodology (lead); Resources (equal); Writing – review & editing (equal). **Bas W. van Oudheusden:** Funding acquisition (equal); Resources (equal); Writing – review & editing (equal). **Marius Swoboda:** Funding acquisition (lead).

DATA AVAILABILITY

The data that support the findings of this study are available from the corresponding author upon reasonable request.

REFERENCES

- ¹A. Hergt, P. Grothe, P. Flaszynski, R. Szwaba, M. Piotrowicz, P. Kaczynski, B. Tartinville, and C. Hirsch, "Transition location effect on shock wave boundary layer interaction, wp 3 internal flow compressors," in *Notes on Numerical Fluid Mechanics and Multidisciplinary Designbook Series (NNFM, Volume 144)* (Springer Nature, 2020), Vol. 144, pp. 229–296.
- ²A. Hergt, J. Klinner, J. Wellner, C. Willert, S. Grund, W. Steinert, and M. Beversdorff, "The present challenge of transonic compressor blade design," *J. Turbomach.* **141**, 091004 (2019).
- ³P. L. Nel, A.-M. Schreyer, C. Janke, I. Vasilopoulos, M. Swoboda, A. Hady, and P. Flaszynski, "Effect of transition on self-sustained shock oscillations in highly loaded transonic rotors," *AIAA J.* **62**, 2063–2075 (2024).
- ⁴P. L. Nel, A.-M. Schreyer, F. Schrijer, B. van Oudheusden, and M. Swoboda, "Research configuration to study shock oscillation mechanism in highly loaded transonic fans," (Submitted).
- ⁵P. L. Nel, A.-M. Schreyer, F. Schrijer, B. van Oudheusden, C. Janke, I. Vasilopoulos, and M. Swoboda, "Shock oscillation mechanism of highly separated transitional shock-wave/boundary-layer interactions," *AIAA J.* (in press).
- ⁶*Shock Wave-Boundary-Layer Interactions*, edited by H. Babinsky and J. Harvey (Cambridge University Press, Cambridge, 2011).
- ⁷R. Giepmans, "Flow control for oblique shock wave reflections," Ph.D. thesis (Technical University of Delft, 2016).
- ⁸N. Sandham, "Shock-wave/boundary-layer interactions," RTO-EN-AVT-195 (University of Southampton, 2011).
- ⁹E. Touber and N. Sandham, "Low-order stochastic modelling of low-frequency motions in reflected shock-wave/boundary-layer interactions," *J. Fluid Mech.* **671**, 417–465 (2011).
- ¹⁰B. Ganapathisubramani, N. T. Clemens, and D. S. Dolling, "Large-scale motions in a supersonic turbulent boundary layer," *J. Fluid Mech.* **585**, 369–394 (2007).
- ¹¹M. Wu and M. Martin, "Analysis of shock motion in shock wave and turbulent boundary layer interaction using direct numerical simulation data," *J. Fluid Mech.* **594**, 71–83 (2008).
- ¹²P. Dupont, C. Haddad, and J. F. Debiève, "Space and time organization in a shock-induced boundary layer," *J. Fluid Mech.* **559**, 255–277 (2006).
- ¹³G. Berkooz, P. Holmes, and J. Lumley, "The proper orthogonal decomposition in the analysis of turbulent flows," *Annu. Rev. Fluid Mech.* **25**, 539–575 (1993).
- ¹⁴J. Westerweel and F. Scarano, "Universal outlier detection for PIV data," *Exp. Fluids* **39**, 1096–1100 (2005).
- ¹⁵A. Melling, "Tracer particles and seeding for particle image velocimetry," *Meas. Sci. Technol.* **8**, 1406–1416 (1997).
- ¹⁶A. Sciacchitano and B. Wieneke, "PIV uncertainty propagation," *Meas. Sci. Technol.* **27**, 084006 (2016).
- ¹⁷A. D'Aguzzo, "Physics and control of transonic buffet," Doctoral thesis (TU Delft, Aerodynamics - Aerospace Engineering, 2023).
- ¹⁸F. Bigillon, Y. Niño, and M. García, "Measurements of turbulence characteristics in an open-channel flow over a transitionally-rough bed using particle image velocimetry," *Exp. Fluids* **41**, 857–867 (2006).
- ¹⁹A. J. Smits and J. P. Dussauge, *Turbulent Shear Layers in Supersonic Flow* (Springer Science & Business Media, 2006).
- ²⁰F. Schrijer, A. Sciacchitano, and F. Scarano, "Spatio-temporal and modal analysis of unsteady fluctuations in a high-subsonic base flow," *Phys. Fluids* **26**, 086101 (2014).